



# Effect of Heat Treatment on Microstructure Evolution and Mechanical Properties of Selective Laser Melted Inconel 718 Alloy

Qiang Zhang , Pan Ren, Xiaohui Tu, Yuhong Dai, Xiaojian Wang, and Wei Li

(Submitted January 10, 2019; in revised form July 13, 2019; published online September 5, 2019)

The microstructure characteristics of the selective laser melted Inconel 718 alloy under as-deposited, homogenization + solution + aging (HSA) and solution + aging (SA) conditions were studied. The anisotropy and heterogeneity of mechanical properties under different conditions were also investigated. Under the as-deposited condition, the morphology and size of the grains are heterogeneous. The dendrite structures which grow nearly perpendicular to the molten pool traces, accompanying interdendritic Laves phase, can be observed within the grains. The dendrite structure completely disappeared, and the Laves phases embedded in the interdendritic regions also dissolved into the matrix to precipitate  $\gamma'$  and  $\gamma''$  phases after heat treatments. Fully recrystallized grains were obtained under the HSA condition, while only incomplete recrystallized grains were obtained under the SA condition. However, the characteristics of  $\gamma'$  and  $\gamma''$  phases are very similar under the HSA and SA conditions. Significant improvement in strength after heat treatments was due to the dissolution of undesirable Laves phase and the precipitation of  $\gamma'$  and  $\gamma''$  phases. For all the three conditions, different tensile properties were observed depending on the orientation of the specimens. The scatter of mechanical properties is notable, and heat treatments increased the scatter of mechanical properties.

**Keywords** Inconel 718 alloy, mechanical properties, microstructure, selective laser melting

## 1. Introduction

Nickel-based superalloys have been extensively and successfully used in many industry fields due to their good mechanical properties at room and elevated temperatures. Among the numerous nickel-based superalloys, Inconel 718 alloy is widely used to fabricate the turbine disks, shafts, blades and other high-temperature components (Ref 1, 2). Inconel 718 is a precipitation-strengthened multicomponent, multiphase alloy composed mainly of Ni, Cr, Fe, Nb, Ti, Al and Mo elements, which is mainly strengthened by precipitated  $\gamma''$  ( $\text{Ni}_3\text{Nb}$ ) and  $\gamma'$  ( $\text{Ni}_3(\text{Al,Ti})$ ) phases (Ref 3–5). However, segregation of high-concentration refractory elements such as Nb and Mo often exists in the Inconel 718 parts produced by traditional techniques (Ref 6), and it is difficult to machine due to the excessive tool wear and low material removal rate (Ref 7). Additive manufacturing (AM) is a type of near-net shaping technique to produce three-dimensional parts (Ref 8). Selective laser melting (SLM) is a powder-bed-based AM process for the manufacturing of complex-shaped metallic parts that are

difficult or impossible to fabricate by conventional techniques. The SLM process has shown a great potential in aviation, space and medical fields due to the flexibility in geometric design (Ref 9).

Researches that focused on the processing parameter optimization, microstructure evolution and mechanical properties of selective laser melted Inconel 718 have been carried out. Moussaoui et al. found that an increased volumetric energy density leads to a lower level of porosity (Ref 10). The microstructure of Inconel 718 parts was characterized by the presence of columnar grains, due to the rapid cooling rate of the molten pool (Ref 11). The dendrite structures grow nearly parallel to the build direction, accompanying interdendritic Laves phase and carbide particles within the grains (Ref 11, 12). And an increase in the volumetric energy density gives rise to a microstructure with longer and tighter dendrites that are more oriented along the build direction (Ref 10). The growth direction of the dendrite and the resulted crystal orientation could also be changed by adopting different scanning strategies (Ref 13). Driven by the ultra-high-temperature gradient and ultra-fast cooling rate, the dendrite microstructure of the selective laser melted Inconel 718 is much finer than that of the casting samples (Ref 14). As a result, the mechanical properties of the as-deposited Inconel 718 are superior to the AMS specification values for cast material, but inferior to the wrought material (Ref 12, 15). The presence of hard and brittle Laves phase, and the lack of  $\gamma'$  and  $\gamma''$  phases are the main reasons for the relatively poor mechanical properties (Ref 12, 16). Post-heat treatments are necessary for optimizing the microstructure and further improving the mechanical performance. Appropriate heat treatments for as-deposited Inconel 718 are proved to be effective in mechanical performance optimization, and the strength and ductility comparable to the wrought samples could be obtained (Ref 12, 17, 18). However,

Qiang Zhang, Pan Ren, Xiaohui Tu, Xiaojian Wang, and Wei Li, Institute of Advanced Wear and Corrosion Resistance and Functional Materials, Jinan University, Guangzhou 510632 Guangdong, People's Republic of China; and Yuhong Dai, Shenzhen Sunshine Laser and Electronics Technology Co., Ltd., Shenzhen 518051 Guangdong, People's Republic of China. Contact e-mails: zhangqiang 2017@jnu.edu.cn and yhdai@sunshine-laser.com.

there are still some limitations such as anisotropy and heterogeneity in microstructure and mechanical properties (Ref 19, 20). Johannes et al. found that the horizontally built specimens had better tensile strength and lower strain to failure values compared to the vertically built specimens for as-deposited and heat-treated samples (Ref 17). In Ni's study, they attributed the anisotropy in strength and ductility to the  $\langle 100 \rangle$  fiber texture and columnar grain morphology (Ref 21).

In order to successfully apply the selective laser melted Inconel 718 to the mentioned fields, the guaranteed and repeatable mechanical properties must be achieved. In this work, the microstructure under as-deposited, HSA (homogenization + solution + aging) and SA (solution + aging) conditions was studied. The corresponding tensile properties along the vertical, diagonal and transverse directions were also implemented. Fracture surfaces, as well as the longitudinal sections of the tested specimens, are also investigated. The anisotropy and the scatter of mechanical properties under different heat treatment conditions are discussed.

## 2. Experimental Procedures

The samples were fabricated using a Concept laser M2 machine operated at a power of 200 W with a scanning speed of 1 m/s, laser focus spot size of 50  $\mu\text{m}$  and layer thickness of 30  $\mu\text{m}$ . The process was conducted under the protection of high purity argon. As illustrated in Fig. 1a, the cylindrical specimens with the diameter of 10 mm and the length of 43 mm were

fabricated with the tensile axis being vertical ( $0^\circ$ ), diagonal ( $45^\circ$ ) and transverse ( $90^\circ$ ) to the build direction. And for each direction under different conditions, three tensile specimens were fabricated. The bidirectional scanning with a rotation of ( $90^\circ$ ) between the successive layers was adopted.

The Inconel 718 spherical powder with the diameter ranging from 15 to 50  $\mu\text{m}$  was used as starting material. The chemical composition of the Inconel 718 powder is given in Table 1. The powder was dried in a vacuum oven for 2 h at  $120 \pm 5^\circ\text{C}$  to eliminate the moisture absorption before use.

The HSA and SA heat treatment processes are adopted according to the industrial standard heat treatment for casting and wrought IN718, respectively. The detailed information of the heat treatments is given in Table 2. The tensile specimens were extracted from the selective laser melted cylinders. The geometry and dimension of the tensile specimens are shown in Fig. 1b. The specimens were subjected to room-temperature tensile testing at a constant crosshead displacement rate of 1 mm/min on an Instron-3382 testing machine. The fracture surfaces and longitudinal cross sections of the tested specimens were examined using a scanning electron microscope (Quanta 250 FEG).

The microstructure examinations were performed on the cross sections which are parallel to and perpendicular to the build direction. The reagent (100 ml HCl + 100 ml  $\text{C}_2\text{H}_5\text{OH}$  + 5 g  $\text{FeCl}_3$ ) was used to reveal the microstructures after mounting, grinding and polishing. The microstructures were characterized by using an optical microscope (Leica DF450) and scanning electron microscope (Quanta 250 FEG). The size of the precipitation phase was measured by using an image processing software, based on the pixel counting.

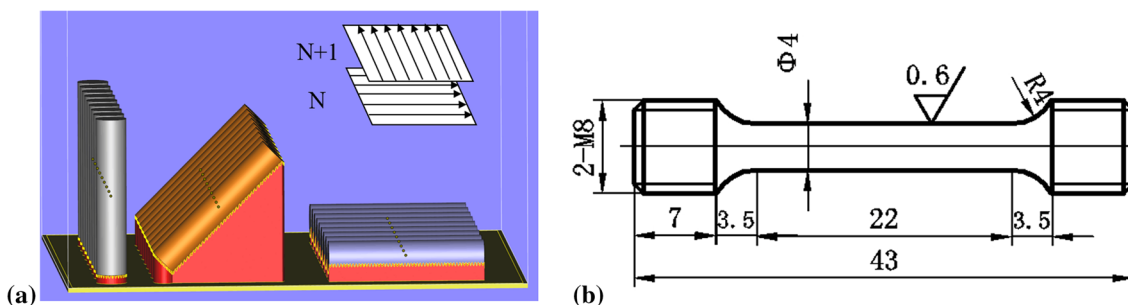


Fig. 1 (a) Illustration of selective laser melted Inconel 718 cylinders with support structure, (b) the sketch of the tensile bar

Table 1 Chemical compositions of the Inconel 718 powder (wt.%)

Element	Cr	Fe	Nb	Mo	Al	Ti	C	Mn	Si	S	Ni
Content	19.29	18.75	5.14	3.12	0.51	0.92	0.037	0.01	0.21	0.003	Balance

Table 2 Heat treatment process

Group	Homogenization treatment	Solution treatment	Aging
As-deposited	...	...	...
HSA	1080 $^\circ\text{C}$ , 1 h/AC	980 $^\circ\text{C}$ , 1 h/AC	720 $^\circ\text{C}$ , 8 h/FC $\rightarrow$ 620 $^\circ\text{C}$ , 1 h/AC
SA	...	980 $^\circ\text{C}$ , 1 h/AC	720 $^\circ\text{C}$ , 8 h/FC $\rightarrow$ 620 $^\circ\text{C}$ , 1 h/AC

AC air cooling, FC furnace cooling

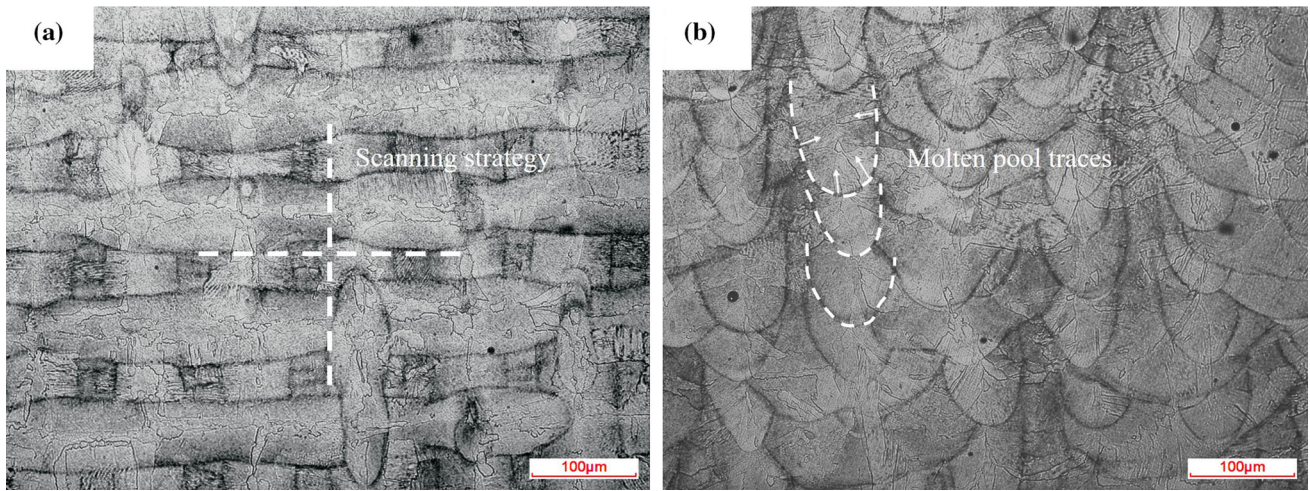


**Fig. 2** Microstructure of the Inconel 718 under the as-deposited condition. (a)  $x$ - $y$  plane, (b)  $y$ - $z$  plane

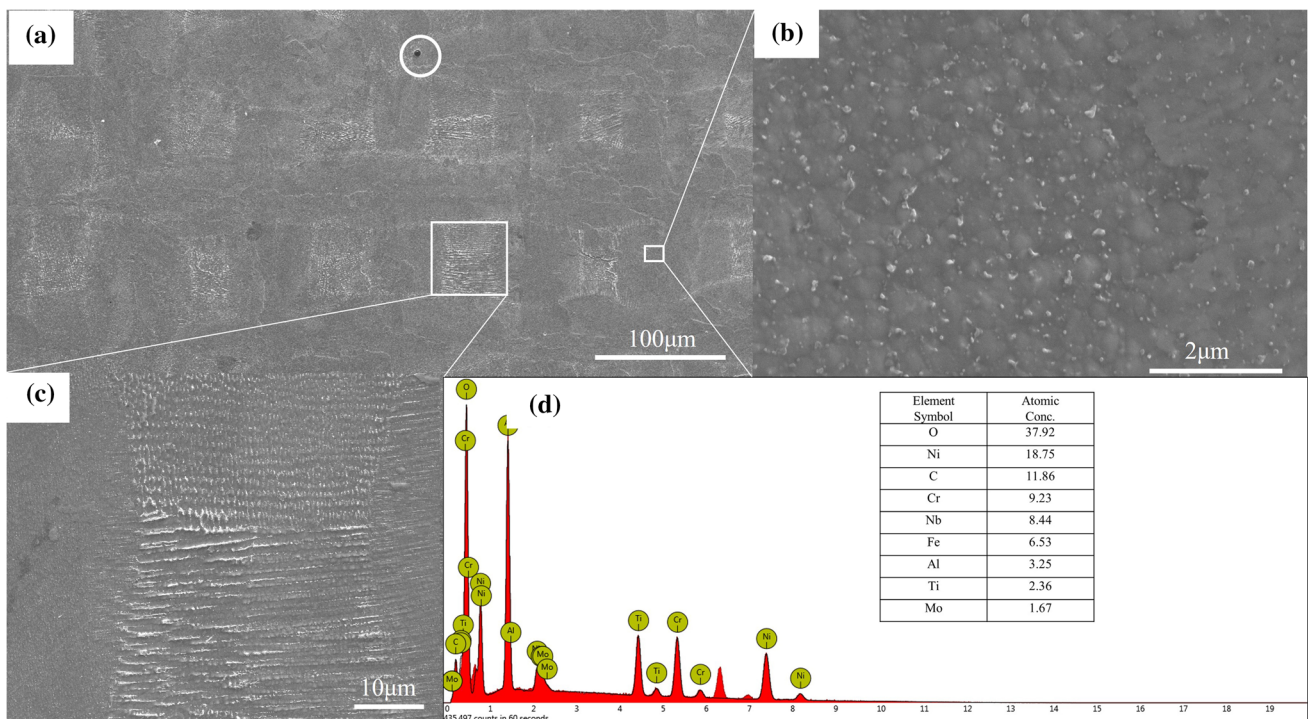


**Fig. 3** Microstructure under the as-deposited condition (a) SEM micrograph showing the chessboard-shaped morphology on the  $x$ - $y$  plane, (b) high-magnification image of the black squares, (c) high-magnification image of the white squares, (d) EDS analysis result of the black round inclusion

The x-ray diffraction (XRD) patterns were obtained using the Rigaku Ultima IV diffractometer with  $\text{CuK}\alpha$  radiation. The diffraction patterns were recorded within the  $2\theta$  range from  $30^\circ$  to  $92^\circ$  with a step size of  $0.02^\circ$ . The density of the selective laser melted samples was quantified according to the Archimedes method (Ref 22). The density of the sample is calculated as follows:

$$\rho = \left( \frac{M_a}{M_a - M_w} \right) \rho_w \quad (\text{Eq 1})$$

where  $M_a$  is the mass of the selective laser melted sample in air,  $M_w$  is the mass of the selective laser melted sample in water and

$\rho_w$  is the density of water. The relative density was calculated by comparing with the density of forged Inconel 718 alloy,  $8.19 \text{ g/cm}^3$  (Ref 23).

### 3. Results and Discussion

#### 3.1 Microstructure under As-Deposited Condition

Optical micrographs of the as-deposited sample in  $x$ - $y$  and  $y$ - $z$  planes are shown in Fig. 2. On the  $x$ - $y$  plane, the scanning strategy used in the present study is clearly visible (Fig. 2a).

Similar morphologies were also reported by other researchers (Ref 24). The morphology and size of the grains are heterogeneous. Fine grain bands along the centerline of the scanning tracks can be observed. This coincides with the EBSD maps for the selective laser melted Inconel 718 in the same scanning strategy obtained by Wan et al. (Ref 13). On the  $y$ - $z$  plane, the molten pool traces are arc-shaped, but the melting depth varies over a wide range, as indicated by the white dash lines in Fig. 2b. The morphologies of the grains are relatively irregular, and some of the grains are not well columnar. As indicated by the white arrows, the growth directions of the grains are not well orientated in the build direction, but perpendicular to the tracks of the molten pool.

A chessboard-shaped morphology can be seen in the SEM micrographs on the  $x$ - $y$  section (Fig. 3a). The high-magnification image shows that the main difference in the black and white squares is the characteristic of Laves phase. In the black

squares, fine granular Laves phase exists (Fig. 3b). In the white squares, irregular stripe Laves phase embedded in the interdendritic regions and grain boundaries can be observed (Fig. 3c). The difference in morphologies may be caused by the different field angles between the section of the image and the growth direction of the epitaxial dendrite, indicating unevenly distributed Laves phase.

The Laves phase forms due to the  $L \rightarrow \gamma + \text{Laves}$  reactions happened at the terminal stage of the solidification process (Ref 25). As well documented, the solidification microstructure is determined by the  $G/V$  ratio, and from a high to low  $G/V$  ratio, the planar, cellular, columnar dendritic and equiaxed dendritic structure can be expected. The cellular structure usually grows in the opposite direction to the temperature gradient (Ref 26). As discussed above, the growth directions of the dendrite structures are not perfectly parallel to the build direction in the present study. This is mainly attributed

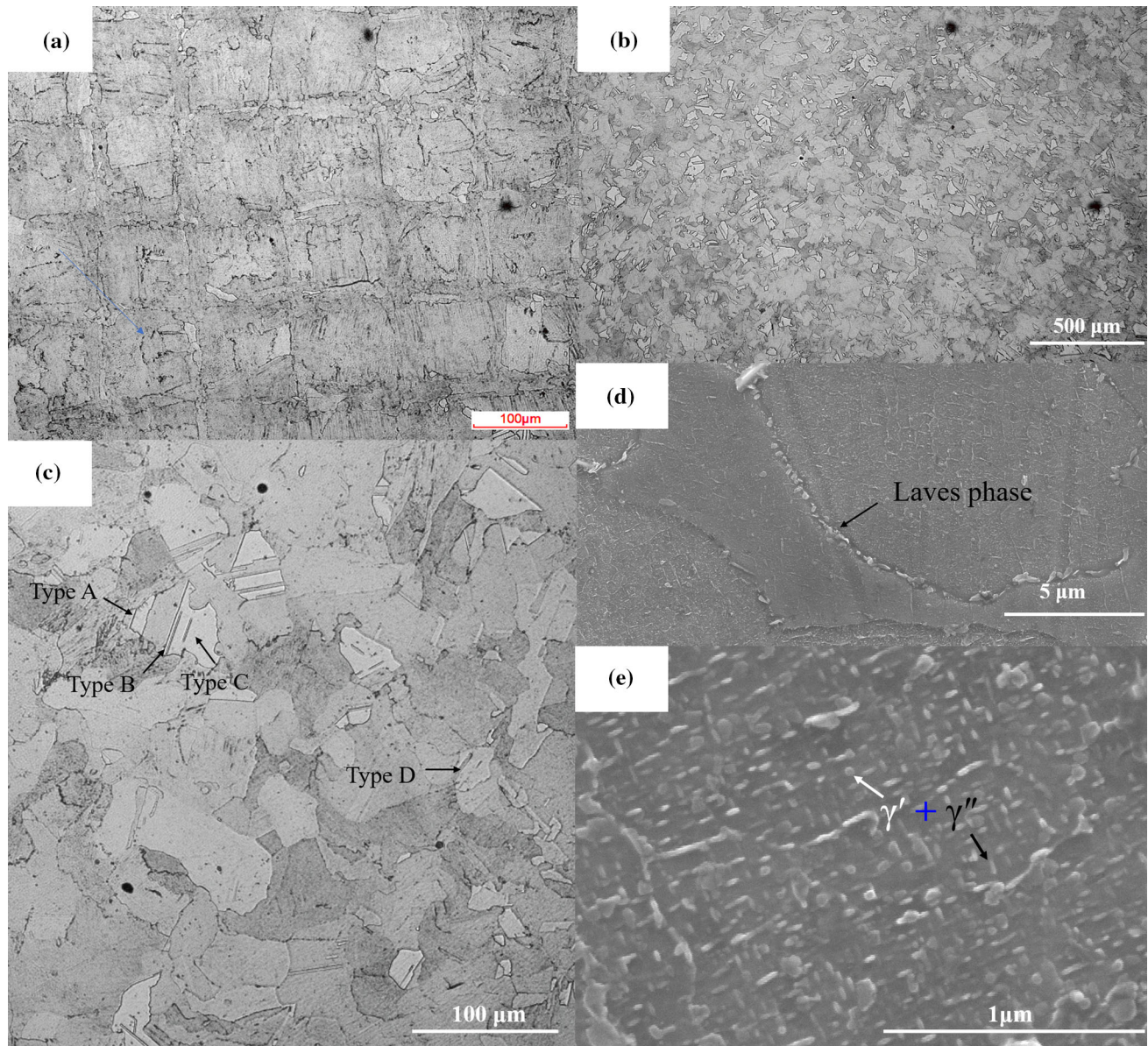


**Fig. 4** Microstructure of the Inconel 718 under HSA condition (a) OM micrograph showing the chessboard-shaped morphology on the  $x$ - $y$  plane, (b) recrystallized grains, (c) annealing twins, (d)(e) magnified images of microstructure

to the formation of the relatively large penetration depth. In a molten pool with a large penetration depth, from the bottom to the top, the temperature gradient changes from parallel to the build direction to perpendicular to the build direction. Therefore, within a single molten pool, the dendrites will grow in different directions, as seen in Fig. 2b. Besides, very few black rounded inclusions can also be observed (Fig. 3a). The EDS analysis revealed that the black inclusions are rich in oxygen and carbon (Fig. 3d).

### 3.2 Microstructure under Heat Treatment Conditions

Figure 4 presents the microstructure of the HSA-treated sample. The chessboard-shaped morphology is clearly visible on the  $x$ - $y$  plane (Fig. 4a), although the homogenization treatment was done at 1080 °C. However, the finer evenly distributed recrystallized grains are obtained, and the molten pool traces are completely invisible on the  $y$ - $z$  plane (Fig. 4b). As shown in Fig. 4c, annealing twins can be observed. According to S. Mahajan's study (Ref 27), annealing twins observed in the recrystallized FCC metals and alloys exhibit four prominent morphologies. As indicated by the black arrows, all the four morphologies exist in the HSA-treated sample. Type A is located in the corner of a grain and Type B is thin and spans opposite sides of the grain. Type C is thicker than B and terminates within the grain. Type D is shallowly inclined to a grain boundary. As shown in the high-magnification images, the solidification dendrite structure and interdendritic Laves phases have disappeared due to the homogeneous treatment (Fig. 4d). The dissolution of interdendritic Laves phase will release Nb and Ti elements into the  $\gamma$  matrix. According to the previous studies,  $\gamma'$  forms in a range

from 600 to 700 °C, and  $\gamma''$  precipitates at temperatures between 700 and 900 °C (Ref 28). As a result, a fairly large number of strengthening phases,  $\gamma'$  and  $\gamma''$ , will precipitate throughout the austenite matrix during the aging heat treatment (Fig. 4e). The  $\gamma'$  and  $\gamma''$  phases could be distinguished by their morphologies (Ref 29). Ultra-fine spherical  $\gamma'$  of  $46 \pm 10$  nm in diameter and disk-like  $\gamma''$  phase with the length of  $81 \pm 18$  nm and the thickness of about  $27 \pm 4.9$  nm were obtained in this study. It should be noted that the Laves phases embedded in the grain boundaries are not completely dissolved since the homogenization temperature is lower than the dissolving point of Laves phase ( $\sim 1165$  °C) (Ref 29). According to the TTT diagram, no distinct  $\delta$  phase precipitation should take place (Ref 30).

As shown in Fig. 5a, the SA-treated sample is very similar in appearance to the HSA-treated sample on the  $x$ - $y$  plane. On the  $y$ - $z$  plane, the molten pool traces are more ambiguous and almost disappeared compared to the as-deposited sample. The columnar grains with smaller grain aspect ratio compared to the as-deposited condition are obtained, which indicates that partial recrystallization has occurred. The magnified image shows that the dendritic structure has completely disappeared (Fig. 5c and d). As indicated by the white arrows, Laves phase and  $\delta$  phase at the grain boundaries can be observed. For the SA-treated sample, the solution temperature is not high enough, so the diffusion of Nb element is inadequate, and the acicular or rod-like  $\delta$  phases will precipitate near the Laves phase at the grain boundaries. Figure 5(d) shows the characteristics of  $\gamma'$  and  $\gamma''$  phases under the SA condition. The characteristics of  $\gamma'$  and  $\gamma''$  phases under the SA condition are very similar to that under HSA condition. The diameter of the ultra-fine spherical  $\gamma'$  is

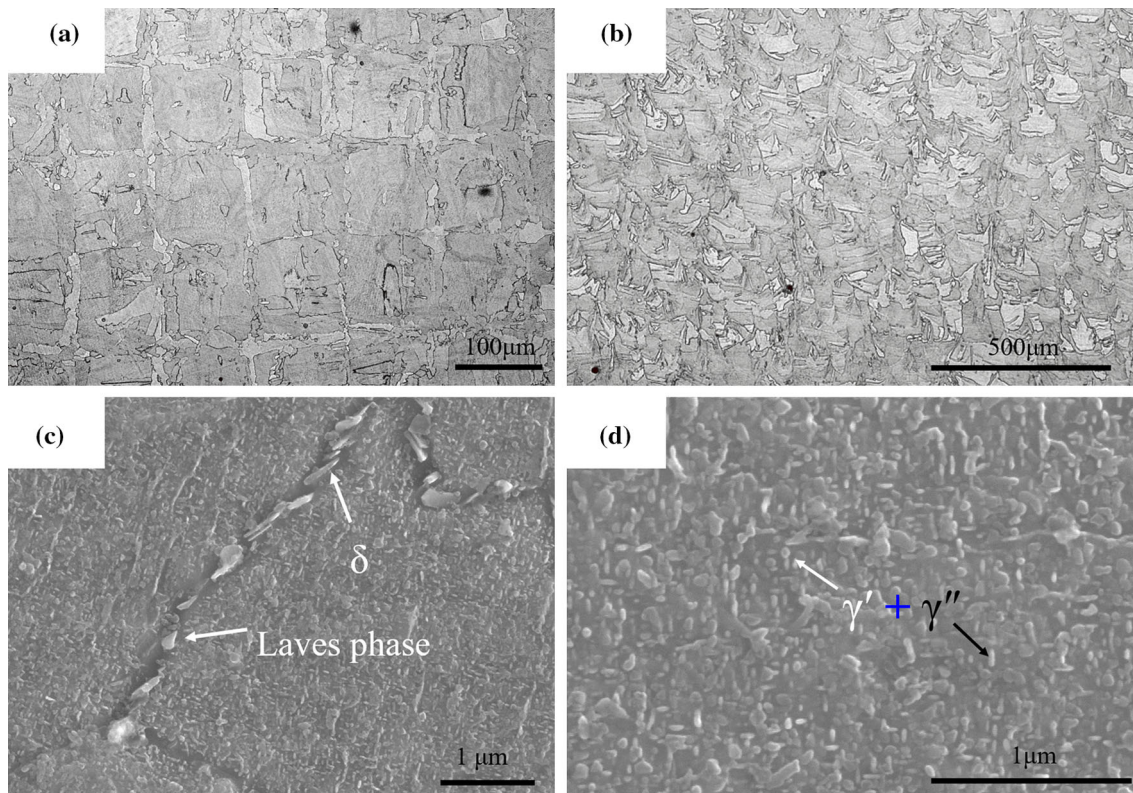


**Fig. 5** Microstructure of the Inconel 718 under SA condition (a) OM micrograph showing the chessboard-shaped morphology on the  $x$ - $y$  plane, (b) recrystallized grains, (c) and (d) magnified images of microstructure

about  $46 \pm 7$  nm. And the length and thickness of the disk-like  $\gamma''$  phase are  $73 \pm 14$  nm and  $27 \pm 5$  nm, respectively.

Figure 6 shows the XRD diffractograms of the samples under different conditions. The XRD patterns suggest the presence of  $\gamma$ ,  $\gamma'$  and  $\gamma''$  phases. No peaks of  $\delta$  phases, carbide or oxide can be observed. This is consistent with the microstructure observations. However, the peaks of  $\gamma'$  and  $\gamma''$  phases could not be distinguished since there is a nearly exact  $\gamma(111)/\gamma'(111)$  peak match as well as matches for  $\gamma(200)/$

$\gamma'(200)/\gamma''(200)$ ,  $\gamma(220)/\gamma'(220)/\gamma''(220)$ , and  $\gamma(311)/\gamma'(311)/\gamma''(033)$  (Ref 31).

### 3.3 Defects

The relative density of the samples under different conditions was measured by Archimedes method. The relative density of the samples under as-deposited, HSA and SA condition is  $98.41 \pm 0.38$ ,  $98.70 \pm 0.12$ , and  $98.59 \pm 0.14$ , respectively. The difference in density under the three conditions is almost negligible, but it still shows some dispersions (Fig. 7a). The details of the shape, size and distribution of the defects were shown in the metallographic images (Fig. 7b and c). Two types of defects, randomly distributed spherical pores and solidification microcracks, along the grain boundaries were identified. The solidification crack is rare in the selective laser melted Inconel 718 alloy, and an example is shown in Fig. 7(c). As indicated in the pictures, the diameter of the spherical pores is about  $30 \mu\text{m}$ , and the length of the solidification crack is about several micrometers. The spherical pores were formed when the gas which comes from the trapped argon or the hollow powder did not escape from the molten pool timely (Ref 10, 32). The sharp angles of the solidification crack could result in local stress concentrations and lead to early fracture. The partially or completely unmelted powders were not observed here.

### 3.4 Mechanical Properties

The typical engineering stress–strain curves for the vertical, diagonal and horizontal directions under different heat treatment conditions, are depicted in Fig. 8. And the tensile property values are listed in Table 3. For all the three

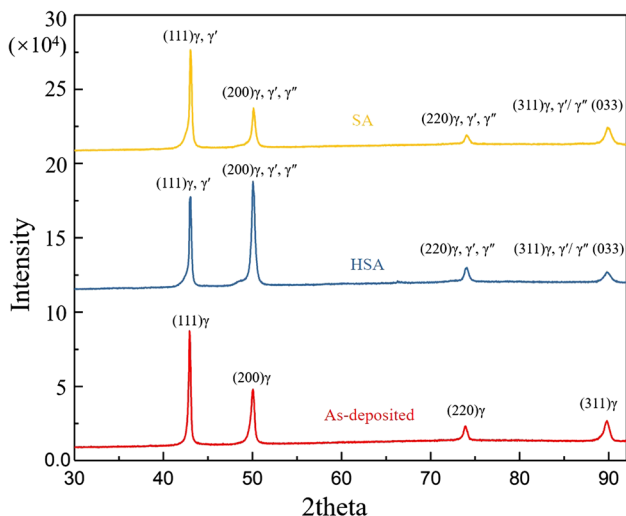


**Fig. 6** The XRD diffractograms of the as-deposited, HSA and SA specimens

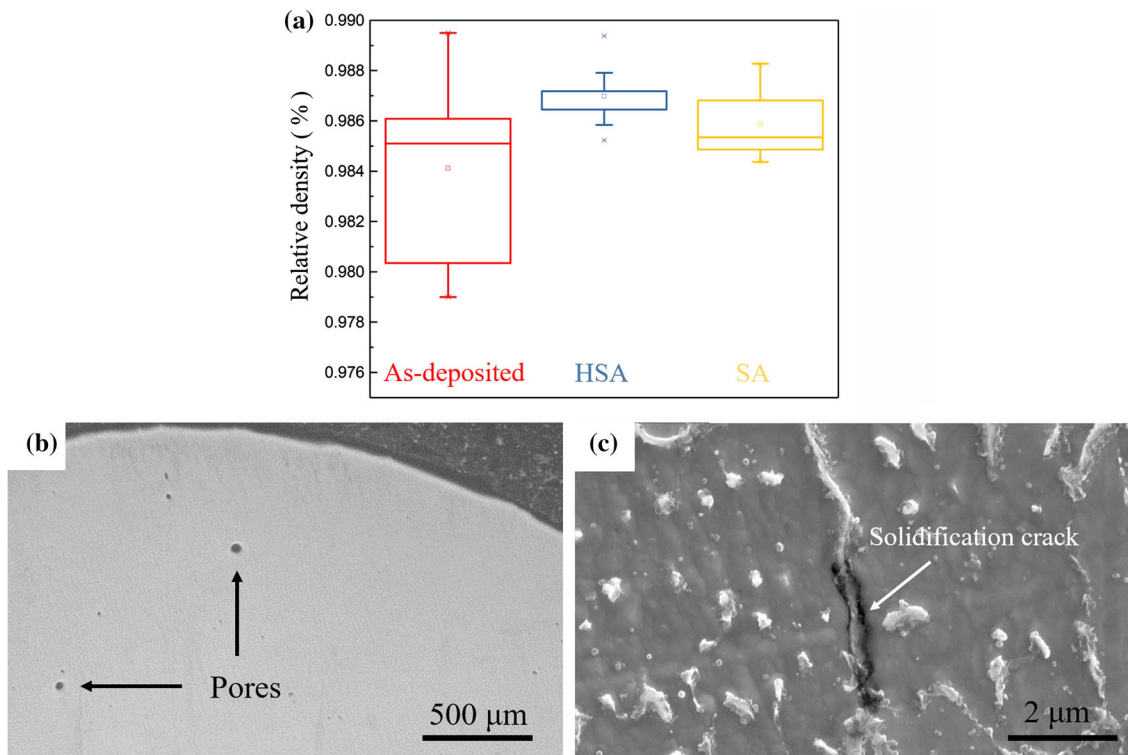


**Fig. 7** (a) The relative density of the samples under different conditions; pores (b) and solidification cracks (c) observed in the as-deposited samples

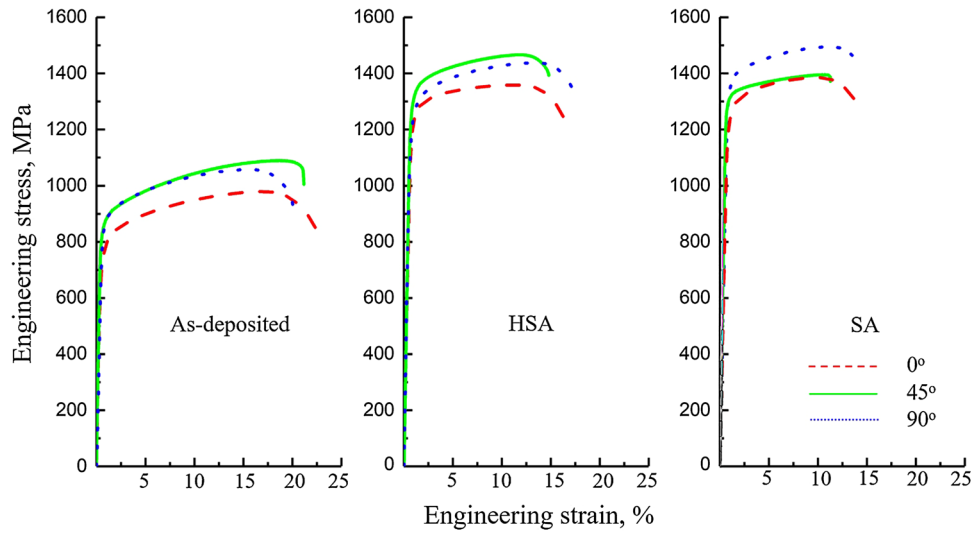


**Fig. 8** The typical engineering stress–strain curves for the vertical, diagonal and transverse directions under different heat treatment conditions

**Table 3** Tensile properties and anisotropy index values of the selective laser melted Inconel 718 alloy under different conditions

Condition	Tensile direction	UTS, MPa	YS, MPa	EL, %	AI-UTS	AI-YS
As-deposited	0°	980 ± 10	734 ± 13	22.3 ± 0.6	6.0	7.2
	45°	1089 ± 28	819 ± 17	22 ± 1		
	90°	1067 ± 21	837 ± 25	22 ± 2		
HSA	0°	1361	1195	14	4.2	5.3
	45°	1453 ± 20	1274 ± 19	15 ± 1		
	90°	1423 ± 43	1219 ± 24	17 ± 1.7		
SA	0°	1398	1228	15	7.9	6.4
	45°	1374 ± 50	1268 ± 39	14 ± 4.4		
	90°	1505 ± 33	1333 ± 29	14		

conditions, different tensile properties were observed depending on the orientations of the specimens. Under the as-deposited condition, the ultimate tensile strength (UTS) and 0.2 pct yield strength (YS) of the samples in the vertical direction are significantly lower than those in other directions, but the elongation to fracture (EL) is very close. The UTS and YS of the samples under HSA and SA conditions are greatly increased, while the EL is remarkably reduced. Significant improvement in strength after HSA and SA treatments was due to the dissolution of the undesirable Laves phase and the precipitation of  $\gamma'$  and  $\gamma''$  phase (Ref 12). The UTS and YS of the samples in the longitudinal direction are lower compared to those in the transverse direction under the three conditions, whereas the trend is not clear in the diagonal direction. The UTS and YS of the HSA-treated samples are lower than the SA-treated samples in the vertical and the transverse directions, but the trend is opposite in the diagonal direction.

The “anisotropy index” (AI) was used for evaluating the extent of anisotropy under different conditions. It was calculated by Eq 2, and the results are listed in Table 3. According to Eq 2, the AI value of the isotropic material is zero, and the values increase with the increase in the extent of anisotropy (Ref 33).

$$AI = \left[ \frac{(2X_{\max} - X_{\text{mid}} - X_{\text{min}})}{2X_{\max}} \right] \times 100 \quad (\text{Eq 2})$$

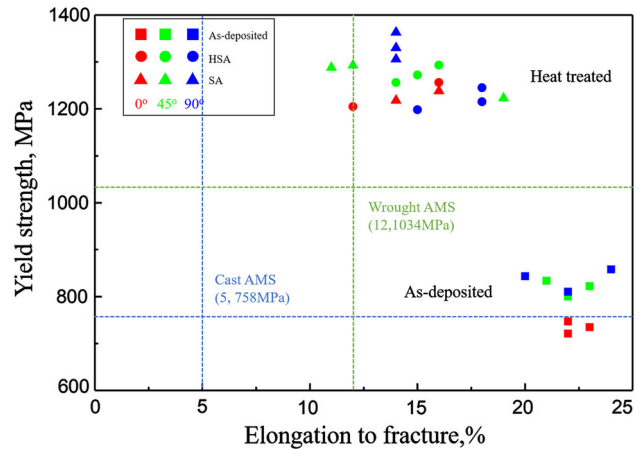


**Fig. 9** Yield strength versus elongation of the selective laser melted Inconel 718 alloy under different conditions

where  $X$  is the average value of the UTS and YS. The results reveal very similar anisotropy for the three conditions. Compared to the as-deposited and SA conditions, the HSA treatment slightly reduced the anisotropy.

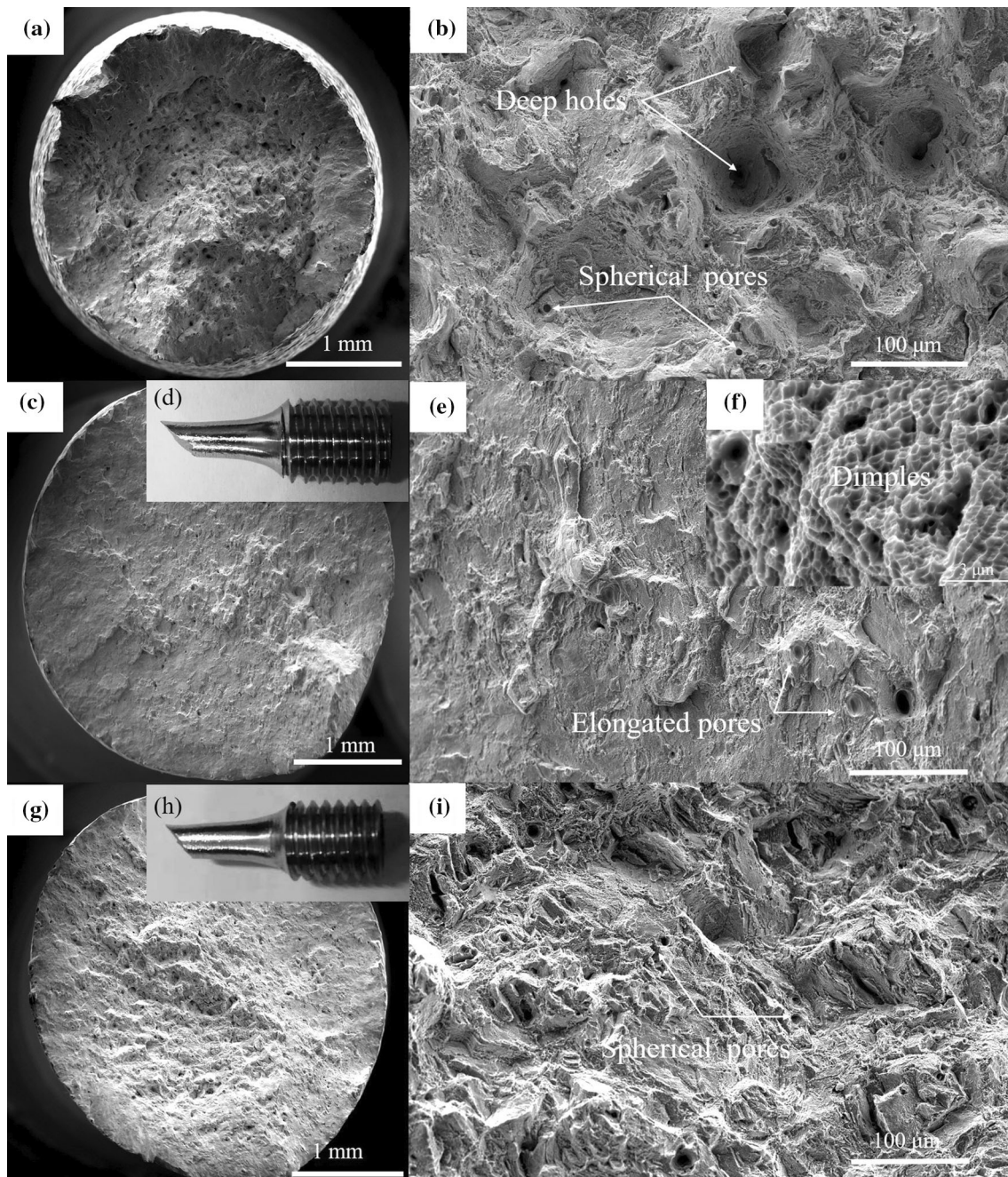


**Fig. 10** Fracture surfaces of the as-deposited specimens: (a) and (b) the longitudinal direction, (c), (d), (e) and (f) the diagonal direction, (g), (h), and (i) the transverse direction

The strength–ductility map (YS versus EL) is given in Fig. 9. The AMS specification values for cast (AMS5383) and wrought (AMS5662) Inconel 718 are included as references (Ref 12). There are notable deviations in the mechanical properties, especially in the ductility. And the lower limit of the mechanical properties could not meet the minimum requirements of the cast or wrought equivalents under some conditions. The scatter in mechanical properties may be attributed to the microstructural heterogeneity (Ref 20). However, it should be noted that both the HSA and SA treatments which were used to eliminate the elements segregation and microstructural heterogeneity, increased the scatter of mechanical properties.

In order to further study the fracture mechanism, the fracture surfaces as well as the longitudinal sections of the tested specimens were examined by SEM. Figure 10 shows the fracture surface of the as-deposited samples. The overall appearance of the fracture surfaces is quite different in the three tested directions, though all the fracture surfaces show transgranular characteristics. For the sample in the vertical direction, the fracture surface contains a fibrous zone and a shear lip zone. The regularly distributed deep holes and randomly distributed spherical pores exist at the fibrous zone (Fig. 10a). There is no obvious level of support that the metallurgical defects give rise to the formation of the deep holes, as indicated in the magnified image (Fig. 10b). The



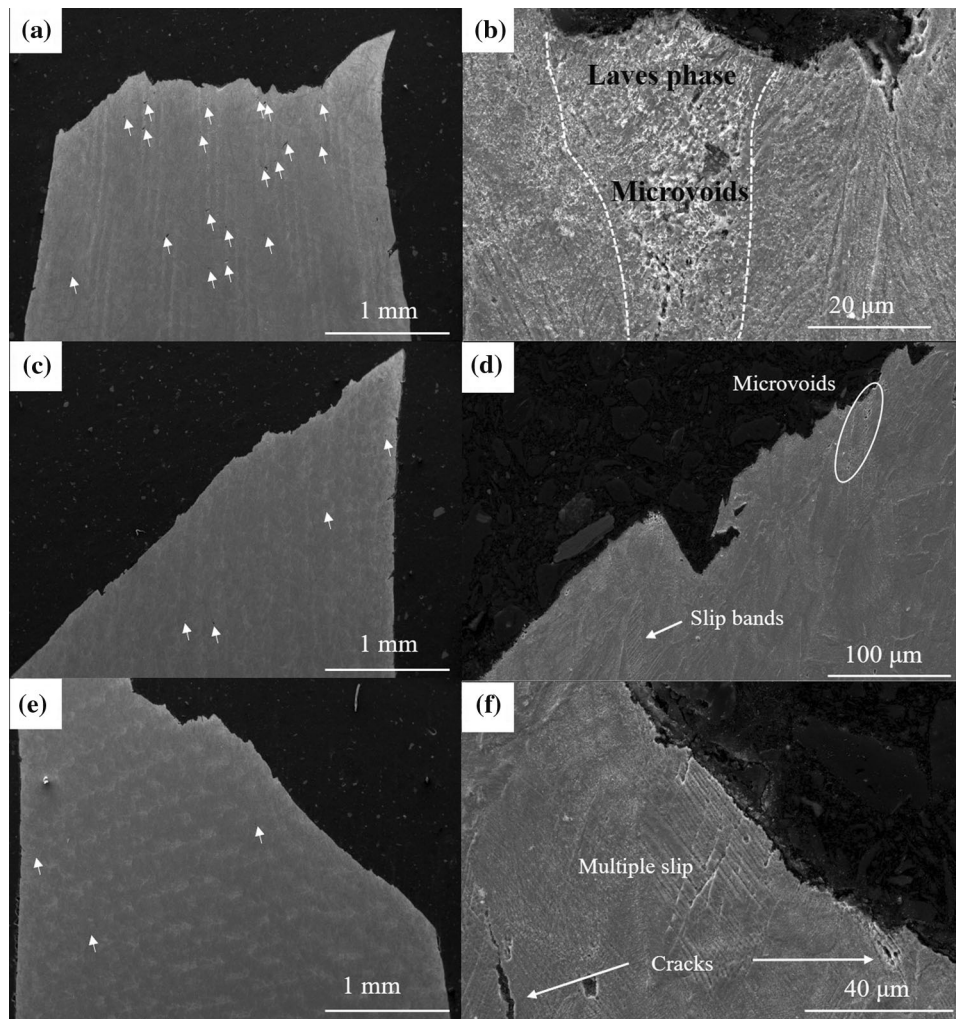


**Fig. 11** The longitudinal sections of the as-deposited samples: (a) and (b) the vertical direction, (c) and (d) the diagonal direction, (e) and (f) the transverse direction

rupture of the specimens in the diagonal and horizontal directions occurred on the surface which is parallel to the maximum shear stress (Fig. 10d and h). And some elongated and spherical pores can be observed on the fracture surfaces (Fig. 10e and i). The different deformation patterns may be related to the geometry, length and orientation of the columnar grains in relation to the tensile direction (Ref 24). As shown in Fig. 10(c) and (g), the fracture surface of the sample in the diagonal direction is rougher than that of the sample in the horizontal direction. The illustration (Fig. 10f) suggests that the relative flat surface is also covered by fine dimples and indicates a transgranular ductile failure mode via microvoids coalescence.

As indicated by the white arrows, there are more microcracks in the vertical sample compared with the diagonal and transverse samples (Fig. 11a, c and e). Severe plastic deformation can be observed on the longitudinal section. And a large number of microvoids exist in the regions containing irregular stripe Laves phase (Fig. 11b). As Sui proposed, long-stripped Laves phases are easy to break up during the tensile process (Ref 34). The deformation of the diagonal and the transverse samples is not as severe as the vertical sample, and slip bands

can be observed within the grains in soft orientations. In Ni's study, they found that Schmid factor of the transverse samples is much smaller than that of the longitudinal samples, which leads to the higher yield stress (Ref 21). In Fig. 11(d) and (f), cracks at the grain boundaries, and voids nucleate and coalescence along the slip bands can be observed.

Similar fracture surfaces and longitudinal sections characteristic of the tested specimens were found for the HSA and SA samples, indicating the same fracture mechanism. The fracture surfaces of the HSA and SA samples, as well as the longitudinal sections of the HSA sample in the vertical direction, are shown in Fig. 12. The appearance of the fracture surfaces is almost the same in the three tested directions under the two different conditions. All the fracture surfaces contain fibrous zone and shear lip zone, which can be attributed to the cup and cone fracture. Being similar to the as-deposited condition, some deep holes can be observed on the surface of the vertical samples (Fig. 12a and g). Similar characteristic can be observed on the longitudinal sections of the samples under different directions, indicating the same deformation mode. The typical characteristics are shown in Fig. 12(b), (d) and (f). The fracture profile is relatively rough and irregular even under low

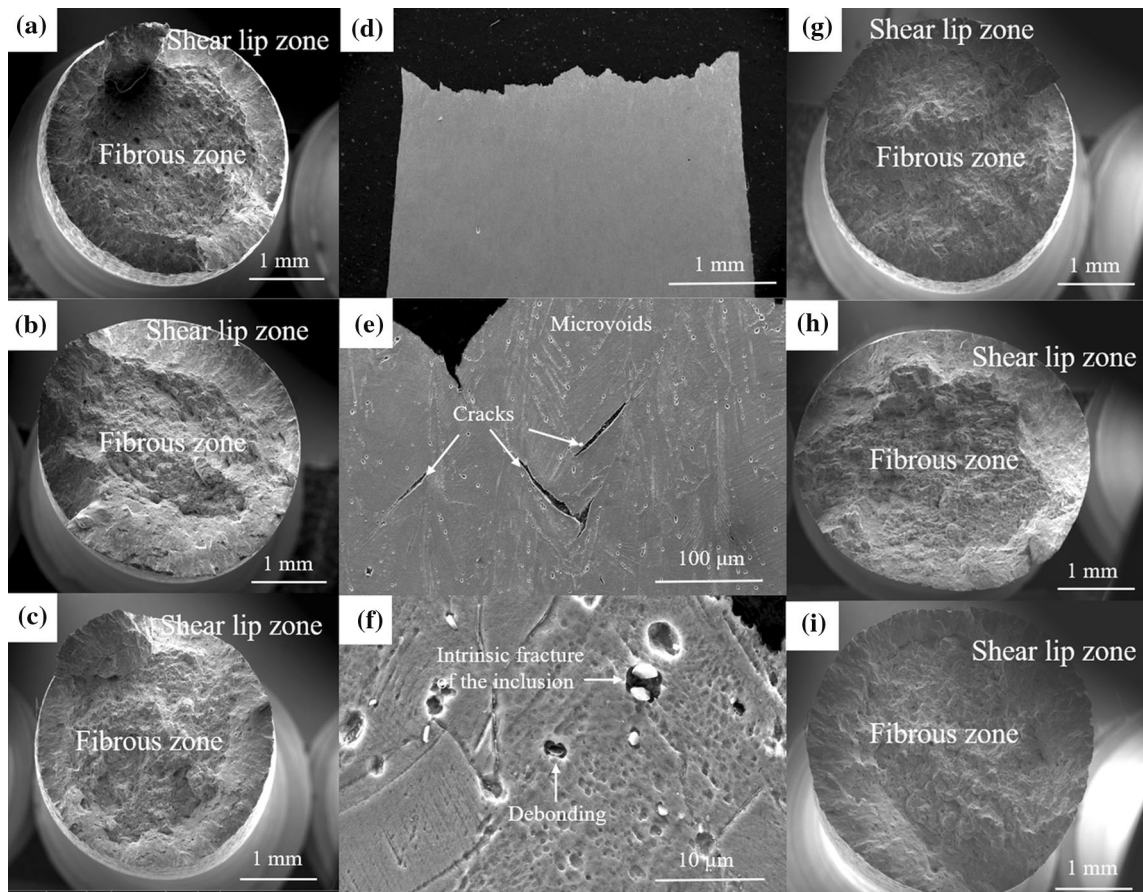


**Fig. 12** (a), (b) and (c) The fracture surfaces of the vertical, diagonal and transverse sample under HSA condition, (d), (e) and (f) the longitudinal sections of the HSA samples in the vertical direction, (g), (h) and (i) the fracture surfaces of the vertical, diagonal and transverse sample under SA condition

magnification (Fig. 12d). Slip bands, microvoids along the slip bands and cracks at the grain boundaries can be observed in Fig. 12e. Moreover, the inclusions which are not observed in the microstructure investigation could also be the source of the microvoids. Both the intrinsic fracture and debonding of the inclusions can lead to the formation of microvoids (Fig. 12f).

As indicated in the fracture analysis, several factors such as microvoids along the slip bands, cracks at the grain boundaries, intrinsic fracture and debonding of the inclusions, as well as the occasionally and randomly distributed preexisting solidification cracks, could lead to fracture. There are several reasons that may contribute to the scatter of mechanical properties. The heterogeneous microstructures, both the grain size and distribution would contribute to the difference in strength (Ref 35). And under the circumstance, the manner of crack initiation and propagation will be difficult to be predicted. The occasionally and randomly distributed preexisting solidification cracks may be another reason for the scatter of mechanical properties. As well documented, the matrix with lower strength usually leads to a larger crack tip plastic zone; thus, the stress concentration in the front of the cracks will be reduced (Ref 36) and delay the formation of the principal crack. This is consistent with the investigations of the longitudinal sections of the broken samples that more microcracks can be observed in the high-strength samples (Figs. 11 and 12). To further reduce the scatter of mechanical properties, the strength and ductility should be balanced.

## 4. Conclusions

In the present study, the microstructure characteristics of the selective laser melted Inconel 718 alloy under the as-deposited, HSA and SA conditions were studied. The anisotropy and scatter of mechanical properties under different conditions were also investigated. The primary conclusions are as follows:

1. The selective laser melted Inconel 718 alloy under the as-deposited condition exhibits heterogeneous grain morphologies. The dendrite structures which grow nearly perpendicular to the molten pool traces, accompanying interdendritic Laves phase, can be observed within the grains.
2. The columnar grains under the as-deposited condition were replaced by fully recrystallized grains after HSA treatment, but incomplete recrystallized grains after SA treatment. The dendrite structure has completely disappeared, and the Laves phases embedded in the interdendritic regions also dissolve into the matrix to precipitate  $\gamma''$  and  $c'$  phases. The difference in characteristics between  $c'$  and  $c''$  phases under the HSA and SA conditions is negligible.
3. For all the three conditions, the different tensile properties were observed depending on the orientations of the specimens. Significant improvement in strength after HSA and SA treatment was due to the dissolution of the

undesirable Laves phase and the precipitation of  $\gamma'$  and  $\gamma''$  phases.

4. The scatter of the mechanical properties is notable. The HSA and SA treatments increased the scatter of the mechanical properties. To further reduce the scatter of the mechanical properties, the strength and ductility should be balanced.

## Acknowledgments

This work was supported by Supported by National Key R&D Program of China (2017YFB0305100) and Fundamental Research Funds for the Central Universities (Grant No. 21618325).

## References

1. K.N. Amato, S.M. Gaytan, L.E. Murr, E. Martinez, P.W. Shindo, J. Hernandez, S. Collins, and F. Medina, Microstructures and Mechanical Behavior of Inconel 718 Fabricated by Selective Laser Melting, *Acta Mater.*, 2012, **60**, p 2229–2239
2. F.C. Liu, X. Lin, C.P. Huang, M.H. Song, G.L. Yang, J. Chen, and W.D. Huang, The Effect of Laser Scanning Path on Microstructures and Mechanical Properties of Laser Solid Formed Nickel-Base Superalloy Inconel 718, *J. Alloys Compd.*, 2011, **509**, p 4505–4509
3. S.S. Babu, N. Raghavan, J. Raplee, S.J. Foster, C. Frederick, M. Haines, R. Dinwiddie, M.K. Kirka, A. Plotkowski, Y. Lee, and R.R. Dehoff, Additive Manufacturing of Nickel Superalloys: Opportunities for Innovation and Challenges Related to Qualification, *Metall. Mater. Trans. A*, 2018, **49**(9), p 3764–3780
4. R.C. Roger, *The Superalloys: Fundamentals and Applications*, 2012
5. Y.T. Chen, A.C. Yeh, M.Y. Li, and S.M. Kuo, Effects of Processing Routes on Room Temperature Tensile Strength and Elongation for Inconel 718, *Mater. Des.*, 2017, **119**, p 235–243
6. G.A. Rao, M. Srinivas, and D.S. Sarma, Effect of Oxygen Content of Powder on Microstructure and Mechanical Properties of Hot Isostatically Pressed Superalloy Inconel 718, *Mater. Sci. Eng. A*, 2006, **435**, p 84–99
7. D.H. Smith, J. Bicknell, L. Jorgensen, B.M. Patterson, N.L. Cordes, I. Tsukrov, and M. Knezevic, Microstructure and Mechanical Behavior of Direct Metal Laser Sintered Inconel Alloy 718, *Mater. Charact.*, 2016, **113**, p 1–9
8. W.D. Huang and X. Lin, Research Progress in Laser Solid Forming of High-Performance Metallic Components at the State Key Laboratory of Solidification Processing of China, 3D Print, *Addit. Manuf.*, 2014, **1**, p 156–165
9. T. DebRoy, H.L. Wei, J.S. Zuback, T. Mukherjee, J.W. Elmer, J.O. Milewski, A.M. Beese, A. Wilson-Heid, A. De, and W. Zhang, Additive Manufacturing of Metallic Components—Process, Structure and Properties, *Prog. Mater. Sci.*, 2018, **92**, p 112–224
10. K. Moussaoui, W. Rubio, M. Mousseigne, T. Sultan, and F. Rezai, Effects of Selective Laser Melting Additive Manufacturing Parameters of Inconel 718 on Porosity, Microstructure and Mechanical Properties, *Mater. Sci. Eng. A*, 2018, **735**, p 182–190
11. J.P. Choi, G.H. Shin, S. Yang, D.Y. Yang, J.S. Lee, M. Brochu, and J.H. Yu, Densification and Microstructural Investigation of Inconel 718 Parts Fabricated by Selective Laser Melting, *Powder Technol.*, 2017, **310**, p 60–66
12. D.Y. Zhang, W. Niu, X.Y. Cao, and Z. Liu, Effect of Standard Heat Treatment on the Microstructure and Mechanical Properties of Selective Laser Melting Manufactured Inconel 718 Superalloy, *Mater. Sci. Eng. A*, 2015, **644**, p 32–40
13. H.Y. Wan, Z.J. Zhou, C.P. Li, G.F. Chen, and G.P. Zhang, Effect of Scanning Strategy on Grain Structure and Crystallographic Texture of Inconel 718 Processed by Selective Laser Melting, *J. Mater. Sci. Technol.*, 2018, **34**, p 1799–1804
14. D.Y. Zhang, Z. Feng, C.J. Wang, W.D. Wang, Z. Liu, and W. Niu, Comparison of Microstructures and Mechanical Properties of Inconel 718 Alloy Processed by Selective Laser Melting and Casting, *Mater. Sci. Eng. A*, 2018, **724**, p 357–367
15. T. Trosch, J. Stroßner, R. Volk, and U. Glatzel, Microstructure and Mechanical Properties of Selective Laser Melted Inconel 718 Compared to Forging and Casting, *Mater. Lett.*, 2016, **164**, p 428–431
16. S. Sui, J. Chen, X.L. Ming, S.P. Zhang, X. Lin, and W.D. Huang, The Failure Mechanism of 50% Laser Additive Manufactured Inconel 718 and the Deformation Behavior of Laves Phases During a Tensile Process, *Int. J. Adv. Manuf. Technol.*, 2017, **91**, p 2733–2740
17. J. Stroßner, M. Terock, and U. Glatzel, Mechanical and Microstructural Investigation of Nickel-Based Superalloy IN718 Manufactured by Selective Laser Melting (SLM), *Adv. Eng. Mater.*, 2015, **17**, p 1099–1105
18. Z.M. Wang, K. Guan, M. Gao, X.Y. Li, X.F. Chen, and X.Y. Zeng, The Microstructure and Mechanical Properties of Deposited-IN718 by Selective Laser Melting, *J. Alloys Compd.*, 2012, **513**, p 518–523
19. J.J. Lewandowski and M. Seifi, Metal Additive Manufacturing: A Review of Mechanical Properties, *Annu. Rev. Mater. Res.*, 2016, **46**, p 151–186
20. Y. Kok, X.P. Tan, P. Wang, M.L.S. Nai, N.H. Loh, E. Liu, and S.B. Tor, Anisotropy and Heterogeneity of Microstructure and Mechanical Properties in Metal Additive Manufacturing: A Critical Review, *Mater. Des.*, 2018, **139**, p 565–586
21. M. Ni, C. Chen, X.J. Wang, P.W. Wang, R.D. Li, X.Y. Zhang, and K.C. Zhou, Anisotropic Tensile Behavior of In Situ Precipitation Strengthened Inconel 718 Fabricated by Additive Manufacturing, *Mater. Sci. Eng. A*, 2017, **701**, p 344–351
22. H.F. Gu, H.J. Gong, D. Pal, K. Rafi, T. Starr, and B. Stucker, Influences of Energy Density on Porosity and Microstructure of Selective Laser Melted 17-4PH Stainless Steel, *J. Exp. Psychol. Gen.*, 2007, **136**, p 23–42
23. D.H. Kim and C.M. Lee, A Study of Cutting Force and Preheating-Temperature Prediction for Laser-Assisted Milling of Inconel 718 and AISI, 1045 Steel, *Int. J. Heat Mass Transf.*, 2014, **71**, p 264–274
24. E. Chlebus, K. Gruber, B. Kuznicka, J. Kurzac, and T. Kurzynowski, Effect of Heat Treatment on the Microstructure and Mechanical Properties of Inconel 718 Processed by selective Laser Melting, *Mater. Sci. Eng. A*, 2015, **639**, p 647–655
25. G.A. Knorovsky, M.J. Cieslak, T.J. Headley, A.D. Romig, and W.F. Hammett, Inconel 718: A Solidification Diagram, *Metall. Trans. A*, 1989, **20**, p 2149–2158
26. W. Kurz and D.J. Fisher, *Fundamentals of Solidification*, Trans Tech Publications, 1986
27. S. Mahajan, C.S. Pande, M.A. Imam, and B.B. Rath, Formation of Annealing Twins in f.c.c Crystals, *Acta Mater.*, 1997, **45**, p 2633–2638
28. J.F. Radavich, The Physical Metallurgy of Cast and Wrought Alloy 718, *Metall. Appl.*, 1989, **718**, p 229–240
29. X. Li, J.J. Shi, C.H. Wang, G.H. Cao, A.M. Russell, Z.J. Zhou, C.P. Li, and G.F. Chen, Effect of Heat Treatment on Microstructure Evolution of Inconel 718 Alloy Fabricated by Selective Laser Melting, *J. Alloys Compd.*, 2018, **764**, p 639–649
30. A. Oradei-Basile and J.F. Radavich, A Current TTT Diagram for Wrought Alloy 718, *Superalloys*, 1991, **718**(625), p 325–335
31. G.H. Cao, T.Y. Sun, C.H. Wang, X. Li, M. Liu, Z.X. Zhang, P.F. Hu, A.M. Russell, R. Schneider, D. Gerthsen, Z.J. Zhou, C.P. Li, and G.F. Chen, Investigations of  $\gamma'$ ,  $\gamma''$  and  $\delta$  Precipitates in Heat-Treated Inconel 718 Alloy Fabricated by Selective Laser Melting, *Mater. Charact.*, 2018, **136**, p 398–406
32. W. Tillmann, C. Schaak, J. Nellesen, M. Schaper, M.E. Aydinöz, and K.P. Hoyer, Hot Isostatic Pressing of IN718 Components Manufactured by Selective Laser Melting, *Addit. Manuf.*, 2017, **13**, p 93–102
33. S. Banumathy, R.K. Mandal, and A.K. Singh, Texture and Anisotropy of a Hot Rolled Ti-16Nb Alloy, *J. Alloys Compd.*, 2010, **500**, p 26–30
34. S. Sui, H. Tan, J. Chen, C.L. Zhong, Z. Li, W. Fan, A. Gasser, and W.D. Huang, The Influence of Laves Phases on the Room Temperature Tensile Properties of Inconel 718 Fabricated by Powder Feeding Laser Additive Manufacturing, *Acta Mater.*, 2019, **718**, p 413–427
35. G.E. Bean, T.D. McLouth, D.B. Witkin, S.D. Sitzman, P.M. Adams, and R.J. Zaldivar, Build Orientation Effects on Texture and Mechanical Properties of Selective Laser Melting Inconel 718, *J. Mater. Eng. Perform.*, 2019, **28**(4), p 1942–1949
36. R.O. Ritchie, The Conflicts Between Strength and Toughness, *Nat. Mater.*, 2011, **10**, p 817–822

**Publisher's Note** Springer Nature remains neutral with regard to jurisdictional claims in published maps and institutional affiliations.